Quantification of post-glacier erosion in the European Alps using ^{10}Be and OSL exposure dating

Joanne Elkadi[1], Benjamin Lehmann[2], Georgina King[1], Olivia Steinemann[3], Susan Ivy-Ochs[3], Marcus Christl[3] and Frederic Herman[1]

[1]Institute of Earth Surface Dynamics, University of Lausanne, 1015 Lausanne, Switzerland
[2]INSTAAR and Department of Geological Sciences, University of Colorado Boulder, Boulder, CO 80309, USA
[3]Laboratory of Ion Beam Physics, ETH Zürich, Otto-Stern-Weg 5, 8093 Zürich, Switzerland

Correspondence to: Joanne Elkadi (joanne.elkadi@unil.ch)

Abstract. The retreat of glaciers since the Last Glacial Maximum (LGM) in the European Alps has left an imprint on topography through glacial and non-glacial erosional processes. However, few methods are currently capable of resolving these mechanisms on Lateglacial to Holocene timescales. Quantifying the relative contributions of mountain erosion, during these different climate cycles, is useful for understanding long-term landscape evolution and the links between global climate and erosion. Here, we combine three Optically Stimulated Luminescence (OSL) exposure dating signals with ^{10}Be surface exposure dating to constrain the post-glacier erosion rates of bedrock samples down a vertical transect adjacent to the Gorner glacier in Zermatt, Switzerland. The results reveal erosion rates on the order of 10^{-2} to 10^{-1} mm a^{-1}, in general agreement with other studies in the region, as well as a strong negative correlation between erosion rates and elevation. Finally, at present glacial erosion is assumed to have a greater influence on landscapes, yet a global compilation of both glacial and non-glacial erosion rates in deglaciated environments shows that erosion rates during interglacial times could be equally important.

1. Introduction

The interplay between erosion and climate has sparked debates and inspired research aimed at better understanding the efficacy of various erosion mechanisms on long-term landscape evolution, as well as the role that climate, and its variability, plays in setting these erosion rates (e.g. Zhang et al., 2001; Molnar, 2004; Willenbring and von Blanckenburg, 2010; Lupker et al., 2013; Cogez et al., 2015; Herman et al., 2013; Herman and Champagnac, 2016; Willenbring and Jerolmack; 2016). Globally, continental topography has been shaped partly through erosional processes associated with rivers, glaciers, soils, rock fall and weathering. For high mountain environments specifically, the strong imprint of glacial and non-glacial erosion is observed at mid- to high-latitudes, but their specific mechanisms and respective impacts on the topography remains convoluted (e.g. André, 2002a; Ballantyne, 2002; Koppes and Montgomery, 2009). It is necessary to better quantify this to develop our knowledge of the influence of mountain erosion on the global feedback loop that exists between climate and erosion during glacial and interglacial times.

Currently in alpine environments, glacial erosion and its associated processes is thought to play a dominant role, and thus extensive research has addressed its quantification, as well as the timing of deglaciations (e.g. Hallet et al., 1996; Montgomery, 2002; Ivy-Ochs and Briner, 2014; Herman et al., 2015; 2018; Wirsig et al., 2016a; b; 2017; Ruszkiczay-Rüdiger et al., 2021; Steinemann et al., 2021). In contrast, studies exploring erosion during interglacial times have mainly investigated at catchment-wide erosion rates, yet disentangling the relative

contributions of glacial erosion, bedrock surface erosion and rockfall has been poorly explored (e.g. Hallet et al.,
45   1996; Delmas et al., 2009; O'Farrell et al., 2009; Guillon et al., 2015; Cook et al., 2020).

In this study, we apply the recently developed approach from Lehmann et al. (2019), that combines Terrestrial
Cosmogenic Nuclide (TCN) dating with Beryllium-10 ([10]Be) and Optically Stimulated Luminescence (OSL)
surface exposure dating, to investigate bedrock post-glacier erosion rates for six samples down a vertical transect
50   adjacent to the Gorner glacier near Zermatt, Switzerland. Then, we examine any potential trends between elevation
or slope with post-glacier erosion rates and find a strong negative correlation between erosion rate and elevation,
but no correlation between erosion rate and surface slope. Finally, the post-glacier erosion rates from this study
are combined with global studies of both glacial and non-glacial erosion rates to reveal that erosion rates during
interglacial times could be more comparable to glacial erosion rates than originally believed.

55

1.1 Measuring erosion rates in deglaciated environments

At present, there exists a wide range of analytical techniques capable of quantifying bedrock erosion rates across
different time intervals (please refer to Moses et al., 2014 and Turowski and Cook, 2017 for in-depth reviews).
60   For timescales on the order of seconds to decades, these methods can include remote sensing (e.g. photogrammetry
on both small and large spatial scales; Inkpen et al., 2000; Dornbusch et al., 2008), or measurements relative to
anthropogenic reference points (e.g. lettering on gravestones; Inkpen and Jackson, 2000). On the other hand,
studies targeting longer timescales ($> 10^3$ years) have measured relative to natural reference points (e.g. resistant
quartz veins; Dahl, 1967; André, 2002b; Nicholson, 2008), exploited the half-lives of different cosmogenic
65   nuclides (e.g. Nishiizumi et al., 1986; Bierman and Caffee, 2002; Balco et al., 2008) or used thermochronometry
(e.g. Reiners and Brandon, 2006; Herman and King, 2018). Unfortunately, there is a lack of available
methodological approaches to quantify bedrock erosion rates across the intermediate time interval, which has
recently driven certain research to devise new methods capable of doing this (Sohbati et al., 2018; Brown and
Moon, 2019; Lehmann et al., 2019).

70

A small number of studies worldwide have already attempted to calculate non-glacial rock surface erosion rates
and have yielded a wide range of results. These include an investigation using TCN in the western US mountain
ranges that estimated the maximum surface erosion rates of alpine bedrock summits at 7.6×10^{-3} mm a^{-1} (Small
et al., 1997), in contrast to another TCN study in the Nepal high Himalayas which instead found erosion rates of
75   8×10^{-2} – 0.2 mm a^{-1} (Heismath and McGlynn, 2007). In Europe, using reference quartz veins in Norway found
erosion rates of 5.5×10^{-4} mm a^{-1} (Nicholson, 2008), while incorporating the edge roundness of boulders in
Scotland produced erosion rates of 3.3×10^{-3} mm a^{-1} (Kirkbride and Bell, 2010). Recent innovative studies
combining TCN and OSL surface exposure dating in the Eastern Pamirs, China, and the Mont Blanc Massif,
France, revealed bedrock surface erosion rates of $<3.8 \times 10^{-5}$ and 1.72×10^{-3} mm a^{-1} (Sohbati et al., 2018) and
80   3.53×10^{-3} – 4.3 mm a^{-1} (Lehmann et al., 2019; 2020) respectively. Finally, a global compilation calculated by
Portenga and Bierman (2011) gave an erosion rate of 1.2×10^{-2} mm a^{-1} by averaging the results from studies that
applied [10]Be to bedrock surfaces. Here, we use a newly developed approach (Lehmann et al., 2019) that combines
two surface exposure dating methods- [10]Be and OSL- to investigate bedrock post-glacier erosion rates and onset
times. In this case, the definition of erosion will be the removal of bedrock surface material.

85

TCN are formed at or near the Earth's surface within specific target minerals as a result of the Earth's constant bombardment by high energy cosmic rays (Dunai, 2010; Gosse and Phillips, 2001). Consequently, following exposure, the concentration of nuclides measured in bedrock can be converted into an exposure age. In this study, we focus on measuring ^{10}Be which is found in quartz. In contrast, OSL is a trapped charge dating technique where

90   a mineral, such as quartz or feldspar, emits light upon light stimulation due to electrons trapped in defects in the mineral's crystal lattice (Huntley et al., 1989; Aitken, 1998). The intensity of the light emitted is an indication of the concentration of trapped electrons. In recent years, the application of OSL to rock surface exposure dating has proved successful in a variety of settings (e.g. Sohbati et al., 2015; Jenkins et al., 2018; Liu et al., 2019; Lehmann et al., 2018) and is based on the principle that, for an exposed surface, the sun's energy is sufficient to naturally

95   empty the surface traps and effectively reduce the luminescence signal to zero (e.g. Sohbati et al., 2011; 2012). This phenomenon is termed "bleaching". Due to the attenuation of light, this bleaching effect decreases exponentially with depth until it become negligible (Habermann et al., 2000; Polikreti et al., 2002, 2003; Laskaris and Liritzis, 2011). Nonetheless, studies have shown that this depth of bleaching increases with exposure time (Habermann et al., 2000; Polikreti et al., 2002, 2003; Laskaris and Liritzis, 2011; Sohbati et al., 2011; 2012;

100   Lehmann et al., 2018; Gliganic et al., 2019) and, after calibration, this bleaching depth can be translated directly into an exposure age for surfaces which have not been affected by erosion (e.g. Lehmann et al., 2018; Sohbati et al., 2018). Recent luminescence instrument developments (Lapp et al., 2015) have facilitated the measurement of rock slices without requiring further mineral separation. This allows multiple luminescence signals, targeted at specific minerals, to be measured from the same slice to obtain the maximum amount of information (e.g. Jenkins

105   et al., 2018; Meyer et al., 2018; Elkadi et al., 2021). Although both TCN and OSL surface exposure dating are influenced by exposure, they are also affected by surface erosion, and if this is not accounted for then it can lead to an underestimation of exposure ages (e.g. Gosse and Phillips, 2001; Lehmann et al., 2019; 2020). The two methods have different sensitivities to erosion (Sohbati et al., 2018; Lehmann et al., 2019) however, since TCN are formed ~50-60 cm (Lal, 1991) below a rock surface whereas bleaching fronts in OSL depth profiles are

110   created only in the top mm to cm (Vafiadou et al., 2007; Sohbati et al., 2011; 2012; Freiseleben et al., 2015). By using these two techniques in conjunction, this difference in sensitivity can be exploited to calculate the surface erosion of bedrock.

1.2 Study area

115

Post-glacier erosion rates were calculated from the flanks of the Gorner glacier, located near the village of Zermatt, Switzerland. This area was chosen due its well constrained glacial history, consisting of a rich collection of geological maps and aerial photos as well as human observations, but also as a result of its proximity to the only other study that applied this method in the local area (Lehmann et al., 2019; 2020) allowing for direct comparisons.

120

Bedrock material was collected from six sampling sites down a vertical transect, with sample lithologies consisting of hornfels, schist and gneiss (Table 1). Reconstructions (Bini et al., 2009) suggest that, aside from the highest elevation sample, the transect was covered in ice during the Last Glacial Maximum and has been de-glaciated since. The three lower elevation samples (GG04, GG05 and GG06) had additional exposure age

125   information from old maps and photos acquired from the Swiss Federal Office of Topography. The three uppermost samples exhibited significant weathering, whereas the three lower elevation samples had extremely well-preserved glacial morphologies and striations (Fig. 1). Samples were collected from bedrock using a

combination of a hammer, chisel and Husqvarna K760 power cutter with a diamond blade. Between two to four
blocks with dimensions of ≈15 cm × 15 cm x 10 cm were extracted at each site, allowing for a sufficient amount

130   of material for both OSL and [10]Be surface exposure dating.

2.   Methodology

2.1 [10]Be sample preparation, measurement and age calculation

135

Sample preparation for [10]Be dating began
with isolating quartz from the bulk rock. To
do this, the uppermost 4 cm of each sample
was crushed and sieved to obtain grain sizes

140   between 250 and 1000 μm, before being
passed through a Frantz magnetic separator
and subsequently treated with HCl and a low
concentration HF solution. Once pure quartz
was isolated and dried, extraction of [10]Be

145   followed the well-established procedure
outlined in Kohl and Nishiizumi (1992) and
Ivy-Ochs (1996). First, the quartz grains
were spiked with 0.25 mg of a [9]Be carrier and
dissolved with supra pure HF (40%).

150   Samples were then purified using two ion
exchange resins to remove unwanted anions
and cations followed by the final selective
pH precipitation of Be(OH)$_2$.[10]Be/[9]Be ratios
of the samples were measured using the 500

155   kV TANDY system at the accelerator mass
spectrometry facility of ETH Zürich,
Switzerland, using the in-house standard
S2007N (Christl et al., 2013) calibrated
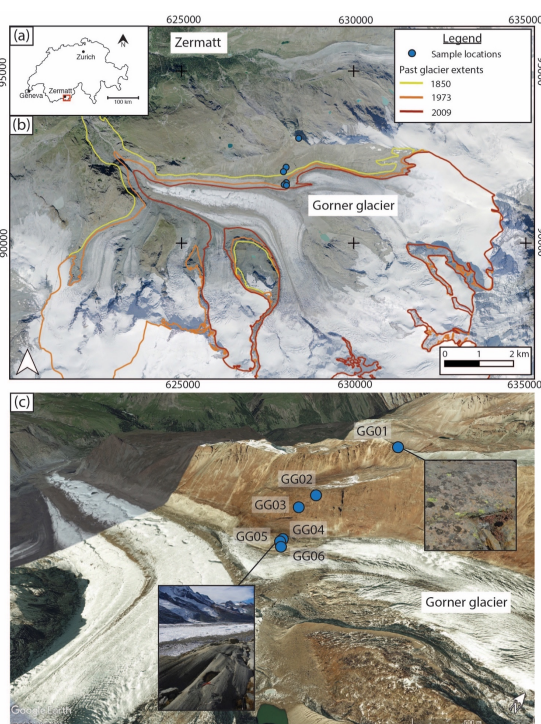against the 07KNSTD standard (Nishiizumi

160   et al., 2007).

Figure 1: Study area and sampling sites on (a) regional, (b) glacier
basin and (c) local scales. Figure 1(b) further depicts the glacier
retreat history obtained from the Global Land Ice Measurements
from Space initiative (GLIMS) (GLIMS Consortium, 2005; Raup et
al., 2007) and 1(c) illustrates the difference in surface preservation
with elevation, and thus exposure age.

Surface exposure ages were determined using a modified version of the CREp online calculator (Martin et al.,
2017; Lehmann et al., 2019) allowing for the application of a non-linear erosion rate correction. The calculations
were done with blank corrected [10]Be/[9]Be ratios (full chemistry long-term laboratory procedural blank of [10]Be/[9]Be

165   (3.2 ± 1.7) x 10^{-15}), the rescaled SLHL Chironico landslide local production rate (4.16 ± 0.10 atoms g^{-1}qtz a^{-1};
Claude et al., 2014) corrected for each sample's latitude, longitude and elevation, the Lifton-Sato-Dunai (LSD)
scaling scheme (Lifton et al., 2014), the ERA40 atmospheric model (Uppala et al., 2005) and the Lifton VDM
2016 geomagnetic database (Pavon-Carrasco et al., 2014 for ages between 0 and 14 ka; GLOPIS-75, Laj et al.,
2004 for ages between 14 and 74 ka). Further information regarding the input data can be found in Table 1.

2.2 OSL

2.2.1 Sample preparation and measurement

Luminescence sample preparation followed the method described in Lehmann et al. (2018) and was carried out at the University of Lausanne, Switzerland. Following collection, samples were immediately placed into black, light obstructing bags and all ensuing laboratory work was done under subdued, red-light conditions. Laboratory work began with coring the samples using a water-cooled Husqvarna DM220 drill to extract cores of 10 mm diameter. Multiple cores were taken per sample, and attention was made to drill as far from the edges as possible, to avoid any potential signal resetting that may have occurred during fieldwork, and from areas with minimal lichen cover and red, iron-oxide staining. The cores were then cut into thin slices ($\approx$0.7 mm thickness) using a Buehler IsoMet low-speed saw mounted with a 0.3 mm thick diamond blade and in the presence of a lubricant. The exact thickness of each slice was measured using a TESA Digitcal Caliper to allow precise reconstructions of the luminescence signal with depth.

Luminescence measurements followed the protocol outlined in Table 2, with low heating rates, extended isothermal holding times of samples prior to stimulation (1°C s^{-1} and 100 s respectively) and fragments of the slices placed in metal cups during measurement (Jenkins et al., 2018, Elkadi et al., 2021). All measurements were performed using Risø TL-DA 20 TL-OSL readers (Bøtter-Jensen et al., 2010) equipped with a DASH head (Lapp et al., 2015) and ^{90}Sr/^{90}Y beta source. The environmental dose rate ($\dot{D}$) was calculated from U, Th, K and Rb concentrations of the bulk rock sample determined using ICPMS at Actlabs, Canada, and the DRAC online calculator (Durcan et al., 2015). All the luminescence signals were subsequently screened using three acceptance criteria: (1) maximum error of test dose signal (Tn) < 15%, (2) Tn greater than 3σ above the background signal and (3) monotonic signal decay. Any slices which did not meet these criteria were excluded from further analysis.

Table 2: Protocol used for measuring the luminescence signals in the rock slices.

Stimulation	Filter	Signal	Target mineral
Preheat at 250 °C for 100 s	BG39 + BG3		
IRSL at 50 °C for 200 s	BG39 + BG3	IRSL$_{50}$ Ln	Feldspar
IRSL at 225 °C for 200 s	BG39 + BG3	post-IR IRSL$_{225}$ Ln	Feldspar
OSL at 125 °C for 200 s	U340 7.5 mm	OSL$_{125}$ Ln	Quartz
Test dose 51.75 Gy			
Preheat at 250 °C for 100 s	BG39 + BG3		
IRSL at 50 °C for 200 s	BG39 + BG3	IRSL$_{50}$ Tn	Feldspar
IRSL at 225 °C for 200 s	BG39 + BG3	post-IR IRSL$_{225}$ Tn	Feldspar
OSL at 125 °C for 200 s	U340 7.5 mm	OSL$_{125}$ Tn	Quartz

2.2.2 Constraining the surface exposure dating model

The evolution of a luminescence signal *L(x,t,r')* (dimensionless) into a rock surface for a given depth *x* (mm), time *t* (year) and recombination centre distance *r'* (dimensionless) can be modelled using the differential equation below (Lehmann et al., 2019):

$$\frac{dL(x,t,r')}{dt} = \frac{\dot{D}}{D_0}[1 - L(x,t,r')] - L(x,t,r')\overline{\sigma\varphi_0}e^{-\mu x} - L(x,t,r')se^{-\rho'^{-\frac{1}{3}}r'} + \dot{\varepsilon}(t)\frac{dL(x,t,r')}{dx} \qquad (1)$$

This equation describes the four competing processes occurring following a surface's exposure to daylight: (1) electron trapping as a result of ambient radiation, (2) optical electron detrapping due to daylight exposure (bleaching), (3) athermal electron detrapping of the IRSL signal, most likely from quantum mechanical tunnelling in feldspars (Huntley, 2006; Kars et al., 2008) and (4) surface erosion. Definitions of the symbols can be found in Table 3, and we refer to Lehmann et al. (2019) for further descriptions.

Table 3: Symbols used in the luminescence surface exposure dating model.

Symbol	Unit	Description
L	dimensionless	Luminescence signal
x	mm	Depth
t	a	Exposure time
r'	dimensionless	Recombination centre distance
	Electron trapping	
$\dot{D}$	Gy a^{-1}	Environmental dose rate
D_0	Gy	Characteristic dose
	Optical electron detrapping	
$\overline{\sigma\varphi_0}$	a^{-1}	Decay rate
σ	mm^2	Photoionisation cross section
φ_0	mm^{-2} a^{-1}	Photon flux
μ	mm^{-1}	Light attenuation coefficient
	Athermal electron detrapping	
s	s^{-1}	Frequency factor
ρ'	dimensionless	Recombination centre density
	Erosion	
$\dot{\varepsilon}$	mm a^{-1}	Surface erosion rate

The term describing optical electron detrapping contains two unknown parameters- $\overline{\sigma\varphi_0}$ and μ- which have been shown to vary greatly across different lithologies, minerals and locations (e.g. Sohbati et al., 2012; Lehmann et al., 2018; Ou et al., 2018). Constraining the values of $\overline{\sigma\varphi_0}$ and μ is one of the biggest challenges in luminescence surface exposure dating. One method of doing so is by calibration from the luminescence profiles of independently known exposure age samples, provided that the calibration and unknown age samples are from the same region and preferably of similar mineralogical composition and orientation (Gliganic et al., 2019; Meyer et al., 2018). Previous calibration sources have involved the use of historical records (Lehmann et al., 2018), road cut outcrops (Sohbati et al., 2012) or the creation of a freshly exposed surface that can be resampled at a later date (Gliganic et al., 2019). In this study, we created sample specific calibration samples by exposing fresh surfaces for ~1 year at each sample site, and subsequently exploited the luminescence signal formed within this year of exposure to determine the unknown parameter values. At one site, we were able to collect calibration samples in two different orientations to improve our understanding regarding the influence of orientation on a luminescence profile with depth (Supplementary Materials).

The data were inverted using a Monte Carlo approach to constrain $\overline{\sigma\varphi_0}$, μ and t. Since each unknown age sample has a site-specific calibration sample, the calibration and unknown age samples were solved for simultaneously using the same $\overline{\sigma\varphi_0}$ and μ values. To do this, for each sample, at first a luminescence profile with depth for the unknown age surface was generated using random values of $\overline{\sigma\varphi_0}$, μ and t, and compared to the observed measured profile using a misfit function as follows:

$$\text{misfit}_{unknown} = \sum_{i=1}^{n} \frac{1}{a} \left| \left(\frac{Ln}{Tn}\right)^{(i)}_{meas} - \left(\frac{Ln}{Tn}\right)^{(i)}_{pred} \right| \qquad (2)$$

235

where n is the number of rock slices in a sample, a is the standard deviation of the plateau in the luminescence depth profile determined qualitatively, and $\frac{Ln}{Tn}$ is the luminescence signal for each rock slice where $\left(\frac{Ln}{Tn}\right)^{(i)}_{meas}$ represents the luminescence signal measured in the sample and $\left(\frac{Ln}{Tn}\right)^{(i)}_{pred}$ is the luminescence signal predicted using the random parameter values.

240

This misfit calculation was then also done for the known-age calibration surface with the same values of $\overline{\sigma \varphi_0}$ and μ, although the exact number of days of exposure (≈ 1 year) was used instead of the randomly generated t value applied for the predicted unknown age profile. Next, the sum of the misfits ($\text{misfit}_{combined}$) generated from the two profiles was used to estimate a likelihood value using:

245

$$\mathcal{L} = \exp\left(-\frac{1}{2}\text{misfit}_{combined}\right) \qquad (3)$$

Finally, a rejection algorithm of likelihood < R was applied, where R was a randomly generated value between 0 and 1. A probability density function of $\overline{\sigma \varphi_0}$, μ and t was constructed from the values that were retained. To

250 ensure that the parameter space was sufficiently explored, we ran 1.25×10^8 trials during the Monte Carlo search with $\overline{\sigma \varphi_0}$ values between 10^{-7} and $10^{-5}\,\text{s}^{-1}$, μ between 1 and 3 mm^{-1} and t between 1 and 200 years.

2.3 Estimating erosion rates

255 Since the [10]Be concentrations and OSL depth profiles in a rock surface are both influenced by exposure and surface erosion, an erosion history can be inferred by jointly inverting the [10]Be and OSL data, as described in Lehmann et al. (2019). While the effects of complex, stochastic erosion histories have been investigated (Brown and Moon, 2019), here we assume a simple, step wise erosion history where, at a specific time in the past, the surface goes from experiencing no erosion to an instantaneous onset of fixed rate of erosion. The inversion method

260 tests random pairs of erosion ($\dot{\varepsilon}$) and erosion onset times (t_s) in log space to find the pairs representative of erosion histories which are most likely to successfully reproduce the [10]Be and OSL data measured from the bedrock surfaces. In this study, we tested 10^4 pairs of $\dot{\varepsilon}$ and t_s with a range of possible $\dot{\varepsilon}$ values from 10^{-6} to 10^{-2} mm a^{-1} and t_s values from 10^{-1} to 10^4 a.

Table 1: Summary of samples and measurements. All errors correspond to 1σ and encompass propagated uncertainties from the AMS measurements, blank correction and the local production rate.

Site ID	Latitude	Longitude	Elevation	Lithology	Surface orientation	Thickness	Density	Topographic shielding factor	^{10}Be results	
	WGS 84		(m.a.s.l)			(cm)	(g cm^{-3})		^{10}Be conc. x 10^3 (at/g)	Exposure age (ka)
GG01	45.9984	7.8052	3251	Hornfels	075/53	4	2.75	0.81	75.76 ± 3.65	1.91 ± 0.1
GG02	45.9809	7.8003	2915	Schist	080/55	4	3.00	0.84	388.74 ± 12.63	11.69 ± 0.46
GG03	45.9797	7.7994	2828	Gneiss	100/60	4	2.39	0.81	372.42 ± 11.55	12.24 ± 0.49
GG04	45.9766	7.8003	2659	Gneiss	085/45	4	2.52	0.91	103.22 ± 3.96	3.53 ± 0.17
GG05	45.9763	7.8001	2626	Schist	070/61	4	2.26	0.79	9.19 ± 1.55	0.35 ± 0.06
GG06	45.9761	7.8005	2610	Gneiss	085/45	4	2.32	0.91	88.24 ± 5.71	3.11 ± 0.22

Table 4: Summary of inferred erosion histories across the three luminescence signals.

Site ID	IRSL$_{50}$		OSL$_{125}$		post-IR IRSL$_{225}$		Average erosion rate (mm a^{-1})	± 1σ
	Erosion rate (mm a^{-1})	Minimum erosion onset time (a)	Erosion rate (mm a^{-1})	Minimum erosion onset time (a)	Erosion rate (mm a^{-1})	Minimum erosion onset time (a)		
GG01	3.43E^{-2}	192	3.13E^{-2}	152	7.22E^{-2}	95	4.59E^{-2}	0.02
GG02	1.83E^{-1}	95	Transient state		1.12E^{-2}	690	9.72E^{-2}	0.09
GG03	Transient state		1.15E^{-1}	76	Transient state		1.15E^{-1}	0
GG04			Transient state					
GG05	2.41E^{-1}	17	1.52E^{-1}	15	6.00E^{-2}	19	1.51E^{-1}	0.07
GG06	4.97E^{-2}	22	1.83E^{-1}	19	1.59E^{-1}	17	1.32E^{-1}	0.06

265

270

3. Results

3.1 ^{10}Be ages

275

The ^{10}Be exposure ages, assuming zero correction for erosion, showed no trend with elevation (Table 1). The highest elevation sample (GG01) is younger than suggested from ice thickness reconstructions (Bini et al., 2009), while samples GG02 and GG03 yield ages commensurate with the decay of the Egesen stadial glaciers, which has been dated to 13.0-11.5 ka (e.g. Ivy Ochs et al., 2009; Protin et al., 2019). These results are in agreement with

280 a group of exposure ages calculated from polished bedrock samples at the nearby Triftje glacier (Kronig et al., 2017). The ^{10}Be ages for the three lower elevation samples (GG04, GG05 and GG06) of 0.35-3.52 ka contrast with information obtained from old geological maps and aerial photos, at the Swiss Federal Office of Topography, which show these surfaces were only exposed 22-40 years ago. This implies that the samples suffer from inheritance, which is noteworthy because it would mean that that the Gorner glacier advanced at one point during

285 the Holocene but did not erode the ~ 3 metres necessary to reset the ^{10}Be signal, as one may expect. The occurrence of inheritance in the three lower elevation samples reveals the complicated exposure history these surfaces have experienced, reinforced by studies across the European Alps which imply repeated oscillations in glacier extent during the Holocene following the Egesen stadial (e.g. Hormes et al, 2001; Ivy-Ochs et al., 2009; Kronig et al., 2017; Protin et al., 2019). While glaciers in the European Alps were likely smaller than present day

290 during the middle Holocene (e.g. Solomina et al., 2015), evidence for subsequent re-advances in glacier extent at the Gorner glacier during the Löbben period and Little Ice Age has been determined (Holzhauser, 1995; 2010), as well as at various sites across the European Alps (e.g. Holzhauser, 1995; Ivy-Ochs et al., 2009; Holzhauser, 2010; Schimmelpfennig et al., 2014; Kronig et al., 2017; Protin et al., 2019).

295 **3.2 OSL unknown parameters**

For all the samples, at least three cores were measured for both the unknown age and calibration samples, and visual assessment of the luminescence profiles with depth confirmed that the surfaces had recorded only one exposure event. Furthermore, as expected, all unknown age sample bleaching consistently penetrated to a deeper

300 depth when compared to their corresponding calibration sample.

For all three luminescence signals, the inversion produced probability density functions of the unknown luminescence parameters- with the best suited $\overline{\sigma\varphi_0}$ and μ results for each sample summarised in Table S1. Figure 2 shows an example result of the IRSL$_{50}$ unknown parameter inversions, taken from sample GG06. Overall, the

305 μ values ranged from 0.59 to 2.45 mm^{-1}, 1.24 to 2.55 mm^{-1} and 1.03 to 2.66 mm^{-1} for the IRSL$_{50}$, OSL$_{125}$ and post-IR IRSL$_{225}$ signals respectively. For the $\overline{\sigma\varphi_0}$ values, the values ranged from 9.17 x 10^{-7} to 1.13 x 10^{-6} s^{-1} for IRSL$_{50}$, 1.33 x 10^{-7} to 1.50 x 10^{-6} s^{-1} for OSL$_{125}$ and 1.07 x 10^{-7} to 7.34 x 10^{-7} s^{-1} for post-IR IRSL$_{225}$. As shown in Fig. S1, the $\overline{\sigma\varphi_0}$ solutions are all of comparable magnitude and overlap within 1σ. This is promising as the $\overline{\sigma\varphi_0}$ parameter is region and mineral dependent (Sohbati et al., 2011) and it is expected that samples from the same

310 location share similar values. In contrast, the μ parameter results vary more than anticipated. Although for each sample, aside from sample GG02, the μ values from the three signals all overlap within 1σ, samples of the same lithology down the transect do not have overlapping results. We speculate that the observed spread reflects mineralogical variations (e.g. Meyer et al., 2018).

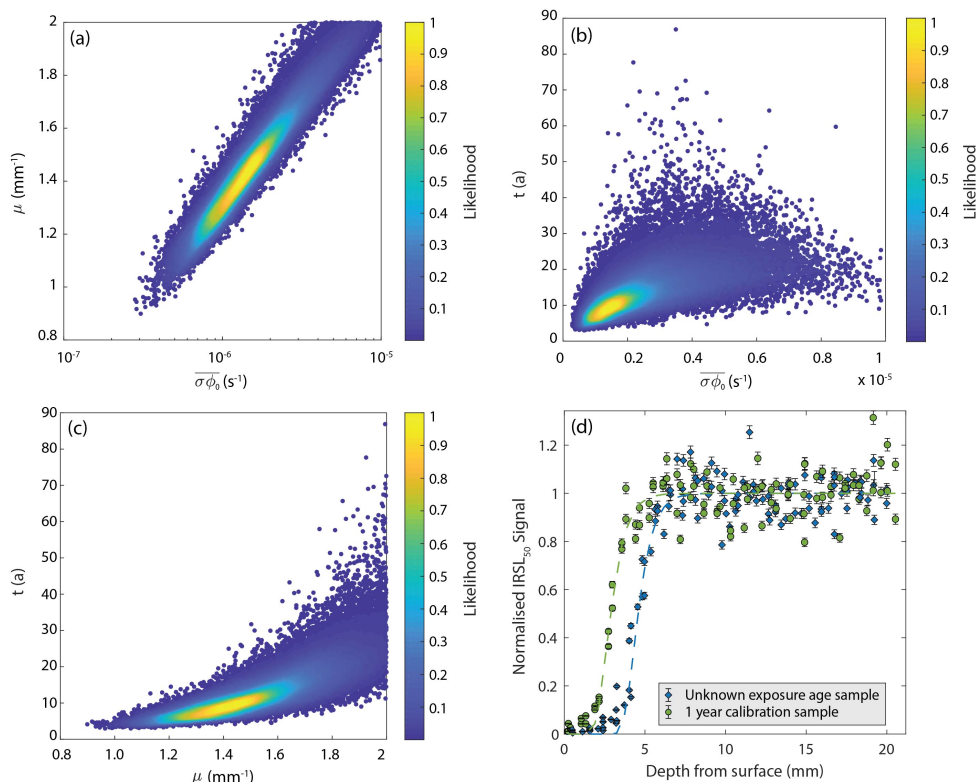**Figure 2: Probability distribution inversion results for the unknown IRSL$_{50}$ parameters $\overline{\sigma\varphi_0}$, μ and t (a-c) and luminescence depth profiles (d) from sample GG06. In the luminescence depth profile, the blue dots represent IRSL$_{50}$ luminescence measurements for the unknown exposure age sample, and the green dots are for the known age calibration sample that was exposed for ~1 year. The dashed lines are the corresponding model fits, using the greatest likelihood $\overline{\sigma\varphi_0}$ and μ values and their respective exposure times. Measurement errors are derived from the square root of the luminescence counts.**

315

3.3 Erosion histories

The inversion outcomes for $\dot{\varepsilon}$ and t_s for all three luminescence signals, following the method described in Sect. 2.4, are reported in Table 4. Since the three lower elevation samples suffered from inheritance rendering the [10]Be 320 ages unusable, exposure age information from the historical maps and photos were employed for the inversion of these surfaces' post-glacier erosion rates using a slightly altered version of the inversion code. Of the six samples, the majority had luminescence profiles in steady state with erosion, thus allowing for the extraction of $\dot{\varepsilon}$ and t_s values. However, some remained in a transient state (e.g. GG04), producing a wider range of erosion rates rendering it difficult to obtain a definite answer, and were therefore excluded from further analysis.
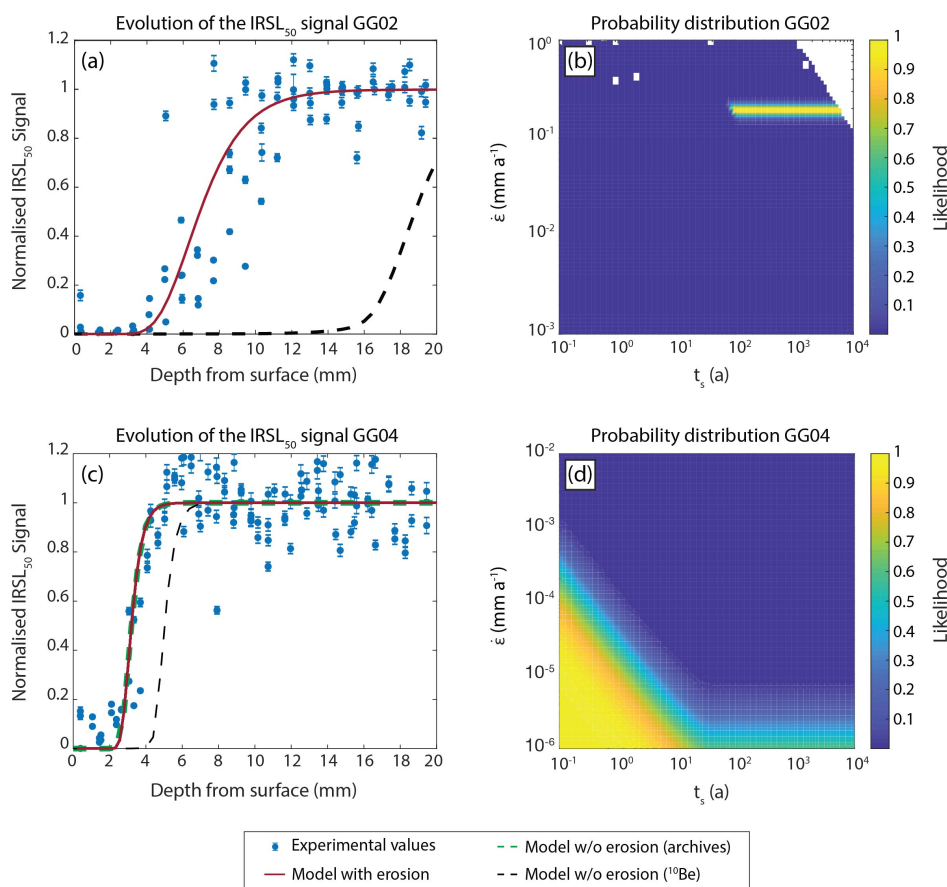
Figure 3: IRSL$_{50}$ luminescence depth profiles and probability distribution inversion results for samples GG02 (a-b) and GG04 (c-d). For the luminescence profiles (a,c) the blue dots represent IRSL$_{50}$ luminescence measurements at that particular depth. Measurement errors are derived from the square root of the luminescence counts. The dashed black line represents the reference profile expected when using the ^{10}Be exposure age, uncorrected for erosion, and the red lines are the inverted solutions using the erosion model and the values of $\dot{\varepsilon}$ and t_s deemed most likely to fit the data. The luminescence depth profile for GG04 (c) also includes a reference profile (dashed green line) when using an exposure age informed from archives of old geological maps and aerial photos. This profile is overlain by the other profiles generated using the erosion model, confirming the information gleaned from the corresponding probability distribution plot that this surface has experienced very low erosion rates. The probability distributions highlight the difference between a sample in steady (b) or transient (d) state with erosion.

325   Luminescence depth profiles and probability density plots of $\dot{\varepsilon}$ and t_s were generated for each sample, and the IRSL$_{50}$ results from samples GG02 and GG04 are shown as examples in Fig. 3. Each luminescence-depth plot includes the experimental data measured from the samples, as well as a reference profile (dashed black line) plotted using solely the ^{10}Be age without correcting for erosion. As seen in Fig. 3, there is a clear mismatch between the depth of the experimental data when compared to that of the ^{10}Be reference plot- in the case of Sample

330   GG02 it translates to a difference in depth of 12 mm. As they both record the same exposure event, this
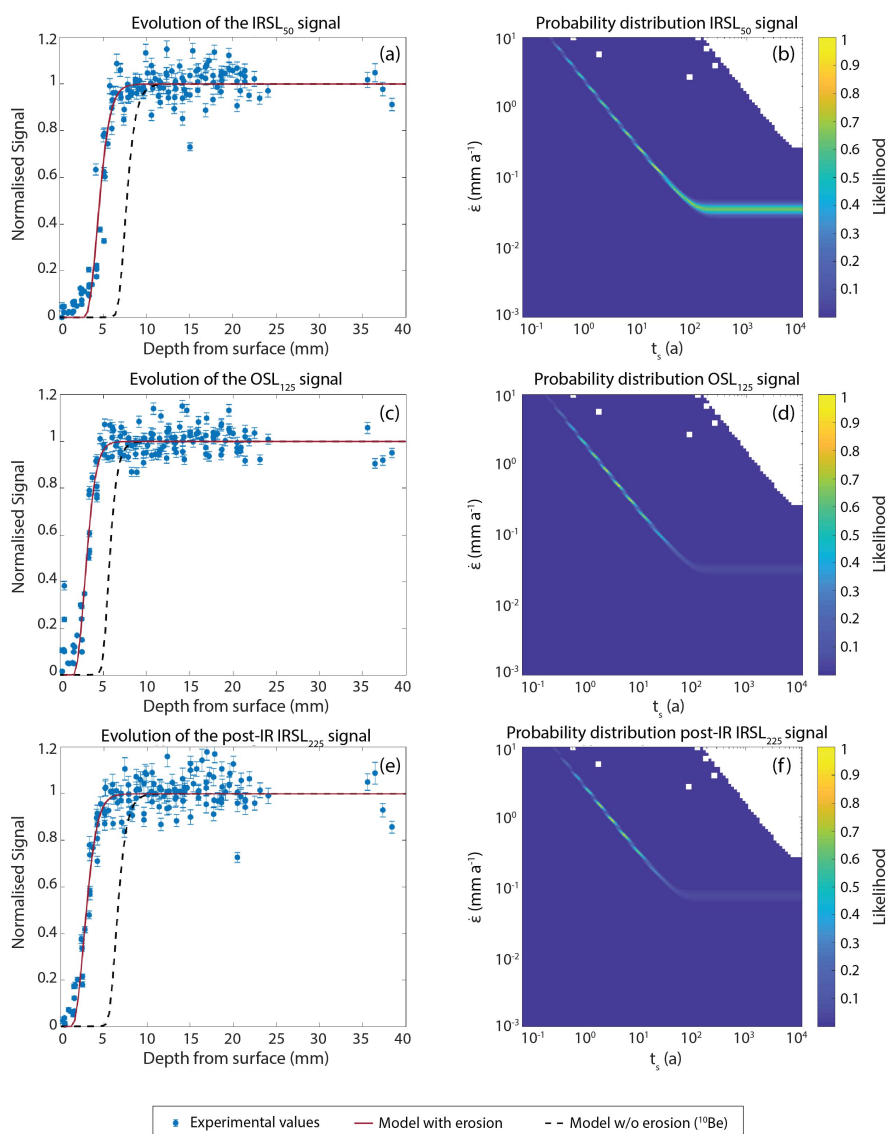
Figure 4: Luminescence depth profiles and probability distribution inversion results for Sample GG01 across the three luminescence signals used in this study- IRSL$_{50}$ (a-b), OSL$_{125}$ (c-d) and post-IR IRSL$_{225}$ (e-f)- which were inverted independently. For the luminescence profiles (a,c,e) the blue dots represent the luminescence measurements at that particular depth. Measurement errors are derived from the square root of the luminescence counts. The dashed black line represents the reference profile expected when using the ^{10}Be exposure age, uncorrected for erosion, and the red lines are the inverted solutions using the erosion model and the values of $\dot{\varepsilon}$ and t_s deemed most likely to fit the data.

discrepancy in depth confirms the presence of surface erosion. When plotting a profile using Equation 1, and the most likely solutions of $\dot{\varepsilon}$ and t_s, it is immediately clear that these are a better fit to the experimental data (red lines).

335   The inverted steady state erosion rates calculated across the three signals are generally consistent- an example
       from Sample GG01 is shown in Fig. 4. Across all the samples, for the IRSL$_{50}$ signal, the rates varied from 3.43 x
       10^{-2} mm a^{-1} to 0.24 mm a^{-1}, OSL$_{125}$ from 3.13 x 10^{-2} mm a^{-1} to 0.18 mm a^{-1} and post-IR IRSL$_{225}$ from 1.12 x 10^{-2}
       mm a^{-1} to 0.16 mm a^{-1}. When looking at the signals individually, the OSL$_{125}$ and post-IR IRSL$_{225}$ results reveal an
       anti-correlation between post-glacier erosion rates and elevation, whereas no trend is observed in the IRSL$_{50}$ data
340   (Fig. 5). Although the luminescence signals target different minerals and traps, they are all still from the same
       sample and thus have experienced the same history. Based on this, an average of the three signals was calculated
       for each site to generate one post-glacier erosion rate value. The trend in erosion rate and elevation observed for
       the OSL$_{125}$ and post-IR IRSL$_{225}$ data is maintained when analysing these erosion averages down the transect (Table
       4).

345

       Combining the inferred $\dot{\varepsilon}$ at steady state with the corresponding minimum t_s, we can calculate the minimum
       amount of material that has been removed from the surfaces as a result of erosion. For all three signals, the results
       indicate that the higher elevation samples have had more material removed than the lower elevation samples. For
       example, the IRSL$_{50}$ data suggest that the highest elevation samples, GG01 and GG02, have had at least 7 mm
350   and 20 mm removed respectively, as opposed to the lower elevation samples, GG05 and GG06, which have lost
       4 mm and 1 mm. This is also supported by the natural texture of the sites.

4. Discussion

4.1 Dominant influences on post-glacier erosion rates

       Several factors, often working in combination with each other, modulate bedrock surface erosion rates. These
       include temperature, elevation and surface slope. A global compilation of ^{10}Be erosion rate measurements from
       bedrock surfaces, integrated over 10^3-10^6 years across various tectonic settings, climate zones and lithologies,
360   failed to find a parameter that strongly dictates outcrop erosion rates (Portenga and Bierman, 2011). This
       contrasted with the results from drainage basin erosion rates, where mean basin slope was revealed to be the most
       dominant factor (Portenga and Bierman, 2011). Conversely, studies in Northern Europe (André, 2002b;
       Nicholson, 2008) calculated post-glacier erosion rates using reference surfaces, and suggested that, in some cases,
       lithology and/or biotic influences have a greater influence on the breakdown of crystalline rocks than
365   environmental or climatic factors.

       To further investigate the potential influences in our study area, the inferred post-glacier erosion rates were plotted
       against elevation and surface slope (Fig. 5). The results exhibit a strong negative correlation between average
       erosion rate and elevation ($r^2 = 0.95$) but no correlation between erosion rate and surface slope ($r^2 = 0.03$). This
370   trend between erosion rate and elevation is in agreement with a study undertaken at the Mont Blanc Massif nearby
       which also found a negative correlation between erosion rate and elevation ($r^2 = 0.53$) that was stronger than the
       positive correlation between erosion rate and slope ($r^2 = 0.22$) (Lehmann et al., 2020). Although the two study
       areas both observe a negative correlation, it is clear from Fig. 5 that the decrease in erosion rate with elevation is
       more pronounced at the Mont Blanc Massif than in this study area. This difference is likely due to local variations
375   influencing the dominant post-glacier erosional mechanisms. Even though the slope of the trends differs, it is

encouraging that the erosion rates from the two studies are comparable and that they both present a negative correlation between elevation and erosion rate.

The anti-correlation between erosion rate and elevation at these two sites is surprising since surfaces at these
380   elevations in mountain environments are typically exposed to frost crack weathering. This occurs when rocks are subjected to temperatures between -3°C and -8°C, termed the frost crack window (FCW) (Anderson., 1998), and we would therefore expect increasing erosion rates with elevation. A similar observation was made by Small et al. (1997), who observed that the bedrock erosion rates from their study, located in an alpine setting, were surprisingly similar to values reported from other environments- excluding arid settings- even though frost crack
385   weathering should be more present. While the presence of snow can help protect the bedrock by maintaining the bedrock surfaces temperature at around 0°C, the lack of correlation between slope and erosion rate for this study site, and the weak correlation at the Mont Blanc Massif, means that frost crack weathering is perhaps not a dominant form of post-glacier erosion in these areas. This is further supported when visually observing the sampling sites, as there is no clear evidence of rockfall scars or surface spallation, suggesting that bedrock erosion
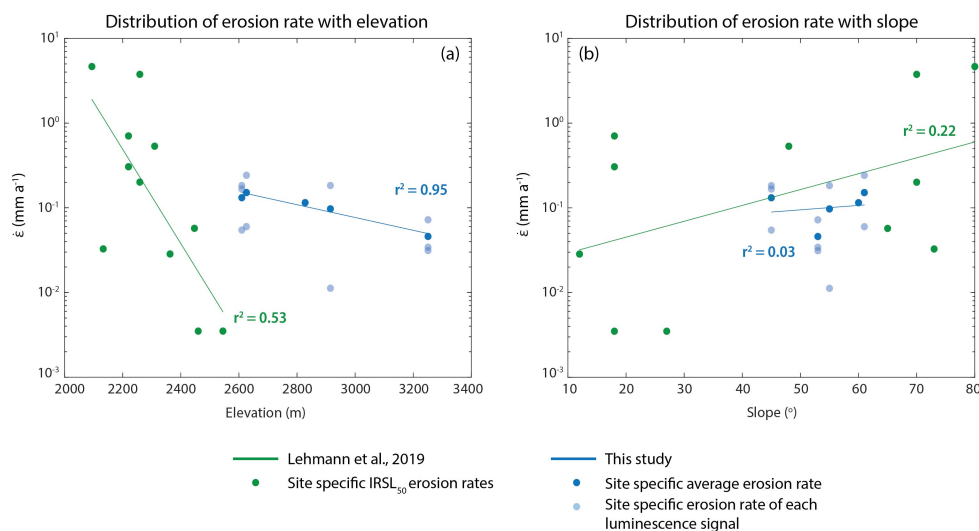390   is most likely occurring through continuous grain-by-grain erosion.

Figure 5: Distribution of inverted bedrock surface erosion rates $\dot{\varepsilon}$ with elevation (a) and surface slope (b). The samples presented in this study are shown in blue (dark blue are the average values, light blue are the individual values from all three luminescence signals) alongside results from a nearby study at the Mont Blanc Massif in green (Lehmann et al., 2019).

Potential explanations for the apparent trend in erosion rate with elevation could include: (1) observed patterns of glacial erosion in valley profiles due to quarrying and/or abrasion both scaling with ice sliding velocity (Harbor, 1992; Fabel et al., 2004; Goehring et al., 2011; Wirsig et al., 2016b; Herman et al., 2021) and the subsequent damaging effect of the variation in ice load on the underlying bedrock (e.g. Leith et al., 2014), (2) wind erosion
395   as a result of katabatic winds coming from the glacier surface, resulting in increased exposure of surfaces near the glacier to wind erosion compared to surfaces higher up the valley sides (Oerlemans and Grisogono, 2002) or (3) the general accumulation of water at lower elevations downslope due to gravity, facilitating erosion mechanisms

that require the presence of water (e.g. frost crack weathering becomes predominantly dependent on the time spent in the FCW once water availability is no longer rate limiting (Anderson, 1998)).

400

4.2 Comparison with other bedrock erosion studies

Attempts to quantify bedrock surface erosion rates from surfaces in glaciated environments, not currently subjected to glacial erosion, have been done worldwide using a variety of techniques integrated across different

405 time scale. TCN methods are generally representative of long-term averages (10^3-10^7 years) (Small et al., 1997; Heimsath and McGlynn, 2007; Portenga and Bierman, 2011), whereas other techniques exist that work on shorter timescales (centennial to millennial), such as comparisons to reference surfaces (André, 2002b; Nicholson, 2008), using the effective radii of curvature of glacial and landslide boulders as a proxy for erosion (Kirkbride and Bell, 2010) or OSL applications (Sohbati et al., 2018; Lehmann et al., 2019; 2020).

410

In the western US mountain ranges, in-situ TCN ^{10}Be and ^{26}Al were used to estimate maximum mean surface erosion rates from alpine bedrock summit surfaces of 7.6 x 10^{-3} mm a^{-1} (Small et al., 1997), while studies in Northwest Scotland, using boulder radii measurements, and Southern Norway, using reference quartz veins, calculated erosion rates of 3.3 x 10^{-3} mm a^{-1} (Kirkbride and Bell, 2010) and 5.5 x 10^{-4} mm a^{-1} (Nicholson, 2008)

415 respectively. Furthermore, a recent study investigating bedrock erosion rates in the Eastern Pamirs of China using OSL depth profiles found minimum steady state erosion rates of <3.8 x 10^{-5} and 1.72 x 10^{-3} mm a^{-1} (Sohbati et al., 2018). These rates are up to four orders of magnitude less than those presented in this study. However, our values are in general agreement with erosion rates reported from studies with climates broadly similar to our study area. These include results from the Nepal high Himalayas, a study which measured bedrock TCN ^{10}Be and ^{26}Al

420 in valley ridge crests and sidewalls and reported erosion rates of 8 x 10^{-2} – 0.2 mm a^{-1} (Heismath and McGlynn, 2007). In Europe, André (2002b) used reference quartz veins, quartzite layers and microcline phenocrysts as reference surfaces to calculate a bedrock surface erosion rate of 0.7 – 5 mm a^{-1}, and a study in the Mont Blanc Massif, applying the same technique as this study, found erosion rates of 3.53 x 10^{-3} – 4.3 mm a^{-1} (Lehmann et al., 2019; 2020). Finally, our results are also in agreement with a compilation of ^{10}Be bedrock measurements

425 which calculated an average global outcrop erosion rate of 1.2 x 10^{-2} mm a^{-1} (Portenga and Bierman, 2011).

Surprisingly, these orders of magnitude are comparable with estimations of sub-glacial erosion rates and a summary of glacial and non-glacial erosion rates worldwide is displayed in Fig. 6. The notion that sub-glacial and periglacial erosion rates are more comparable than previously thought has been suggested previously (O'Farrell

430 et al., 2009; Guillon et al., 2015). Erosion at a glacier bed is primarily executed through abrasion and plucking. Although the latter is thought to be more dominant, it remains difficult to uncouple the two processes with certainty when estimating erosion rates beneath a glacier. Calculations so far have returned rates that differ by several orders of magnitude (Hallet et al., 1996; Koppes et al., 2009; 2015; Herman et al., 2015; 2021), mostly resulting from the sliding velocity of glaciers, but it must also be noted that the various methods are integrated

435 over different timescales depending on the method itself and, for previously glaciated surfaces, on the duration of ice cover in the corresponding study areas. In the European Alps, direct measurements from quartz veins at a glacier snout in the Swiss Alps presented abrasion rates of 0.9 – 3.75 mm a^{-1} (Embleton and King., 1975), while

measurements on marble plates cemented to the glacier bed of the Glacier d'Argentiere, France, gave a rate of 36 mm a^{-1} (Boulton, 1979).
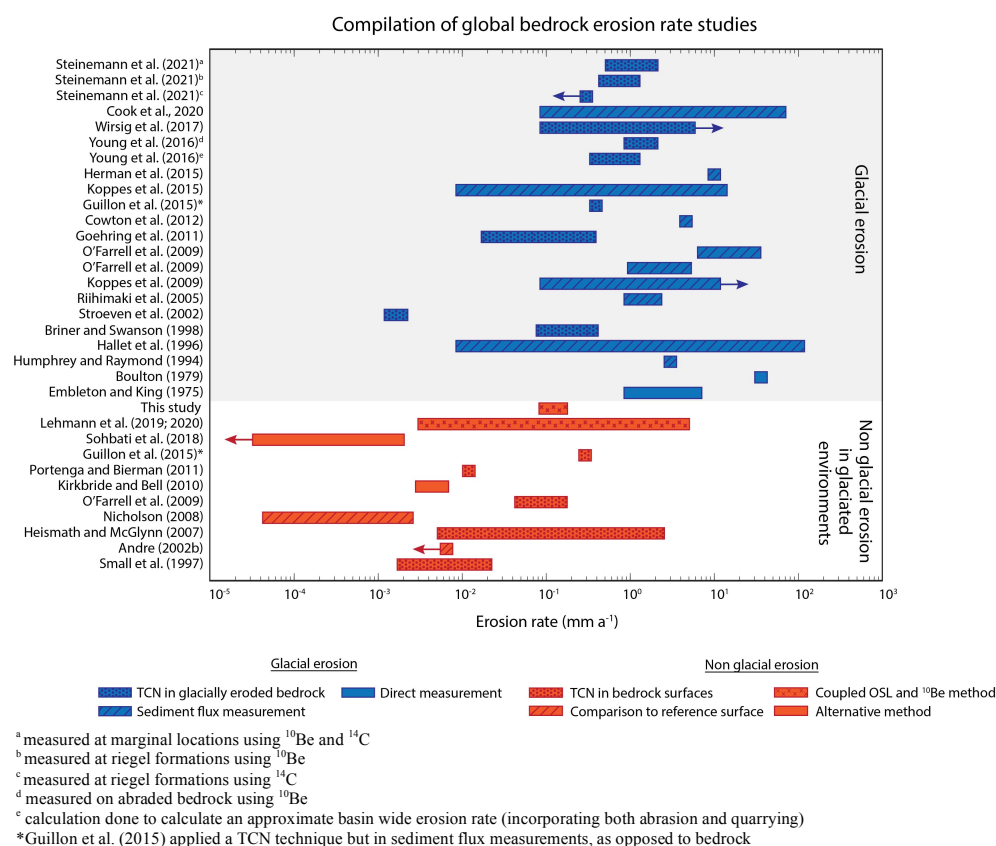

Figure 6: Summary of the results of studies worldwide which have attempted to calculate glacial erosion rates (blue) and non-glacial erosion rates in glaciated environments (red). Results involving bedrock of sedimentary lithology were excluded as they are not comparable to our study area. The arrows represent "greater than" or "less than".

440 Bedrock sub-glacial rates have also been determined for formerly glaciated surfaces by exploiting the difference in half-lives between TCN ^{10}Be and ^{14}C in bedrock. In these studies, sampling deliberately targeted surfaces which displayed no apparent signs of quarrying, to attempt to isolate abrasion rates, and the results produced values between 0.02 and 1.8 mm a^{-1} (Goehring et al., 2011; Wirsig et al., 2016b; 2017; Steinemann et al., 2021). The large range is due to differences in sample locations- the lower erosion rates were taken from marginal positions

445 while higher rates from the glacial trough. From a more global perspective, the application of ^{36}Cl in Washington, USA, found subglacial erosion rates of 0.09-0.35 mm a^{-1} (Briner and Swanson, 1998) and bedrock TCN measurements in Greenland using ^{10}Be yielded rates of 0.39-1.1 mm a^{-1} (Young et al., 2016). In the study done by Young et al. (2016), the authors suggest that their results predominantly reflect sub-glacial abrasion, due to their sampling strategy, and proceed to estimate a likely total basin wide erosion rate of 1 – 1.8 mm a^{-1} by assuming

450 that 30-60 % of a glacier's bedrock erosion budget is attributed to quarrying. An advantage of applying TCN

based measurements to calculate sub-glacial erosion rates is that this allows for the calculation of erosion rates at multiple points, which could subsequently reveal any potential spatial variability in sub-glacial erosion rates.

455 Alternatively, in presently glaciated areas, contemporary sediment volume measurements at, or beyond, a glacier terminus can be coupled with ice velocities to provide insight into glacial erosion rates on a greater catchment scale. In the European Alps, studies applying this have produced values between 0.1 and 1 mm a^{-1} (Hallet et al., 1996), but findings around the globe have occasionally reported higher values (e.g. Koppes et al., 2009; 2015; Cook et al., 2020). For example, in New Zealand, glacier sliding velocities were mapped using remote sensing and combined with sediment flux measurements over 5 months at a glacier front to produce a glacial erosion value
460 of ~10 mm a^{-1} (Herman et al., 2015) while suspended sediment load measurements collected at the Leverett glacier in Greenland over two melt seasons in 2009-2010 produced a sub-glacial erosion rate of 4.6 ± 2.6 mm a^{-1} (Cownton et al., 2012). A full compilation of glacier erosion rates, calculations and methods can be found in Herman et al. (2021). Results from sediment yield studies, and the ensuing interpretations of sub-glacial erosion rates, should be treated with caution as there are elements of the method which introduce potential bias.
465 Nevertheless, the challenge of accessibility to the ice-bed interface beneath a glacier renders it difficult to estimate sub-glacial erosion rates by other means, and sediment flux measurements are often the only data available.

5. Conclusion

470 This study demonstrates the value of combining ^{10}Be and OSL surface dating techniques for quantifying post-glacier bedrock erosion rate histories across time scales on the order of 10^1 to 10^4 years. We extended the method introduced by Lehmann et al. (2019; 2020) by measuring three OSL signals (IRSL$_{50}$, post-IR IRSL$_{225}$ and OSL$_{125}$) for the samples in this study. The results show that using multiple OSL signals can yield, not only additional constraints for the method, but also provide information in the absence of other data- for example, the IRSL
475 signals in Sample GG03 were not in steady state with erosion, and therefore could not be used to calculate an erosion rate, but the OSL$_{125}$ signal could be used.

Averaging the erosion rate results for the three signals at each sample site resulted in post-glacier erosion rates that vary from 9.72 x 10^{-2} to 1.51 x 10^{-1} mm a^{-1}. The magnitude of the erosion rates found here at the Gorner
480 glacier are in agreement with a nearby study at the Mont Blanc Massif (Lehmann et al., 2019; 2020). Plotting the post-glacier erosion rates against elevation and surface slope for the samples in this study indicates a strong anti-correlation of erosion rate with elevation, and no correlation between erosion rate and slope. This is in broad agreement with the results from the Mont Blanc Massif, however the trends there are more pronounced. We suspect this reflects local differences in the dominant post-glacier erosion mechanisms. Finally, a global
485 compilation of both glacial erosion rates, as well as non-glacial erosion rates in glaciated environments, reveals the rates are more comparable than previously assumed, which could lead to important implications for landscape evolution models and assessing the impact of Quaternary climate on mountain erosion.

490

References

Aitken, M.J.: An Introduction to Optical Dating: The Dating of Quaternary Sediments by the Use of Photon-Stimulated Luminescence, Oxford University press, 1998.

495 Anderson, R.S.: Near-Surface Thermal Profiles in Alpine Bedrock: Implications for the Frost Weathering of Rock, Arct. Antarct. Alp. Res., 30, 362-372, 1998.

André, M.-F.: Do periglacial landscapes evolve under periglacial conditions?, Geomorphology, 52, 149-164, 2002a.

500

André, M.-F.: Rates of postglacial rock weathering on glacially scoured outcrops (Abisko-Riksgränsen area, 68°N), Geogr. Ann. A., 84(3-4), 139-150, 2002b.

Balco, G., Stone, J.O., Lifton, N.A., and Dunai, T.J.: A complete and easily accessible means of calculating

505 surface exposure ages or erosion rates from [10]Be and [26]Al measurements, Quat. Geochronol., 3, 174-195, 2008.

Ballantyne, C.K.: Paraglacial geomorphology, Quaternary Sci. Rev., 21, 1935-2017, 2002.

Biermann, P.R., and Caffee, M.: Cosmogenic exposure and erosion history of Australian bedrock landforms,

510 Geol. Soc. Am. Bull., 114(7), 787-803, 2002.

Bini, A., Buoncristiani, J.-F., Couterrand, S., Ellwanger, D., Felber, M., Florineth, D., Graf, H.R., Keller, O., Kelly, M., Schlüchter, C., and Schoeneich, P.: Die Schweiz während des letzteiszeitlichen Maximums (LGM), Bundesamt für Landestopografie swisstopo, 2009.

515

Bøtter-Jensen, L., Thomsen, K.J., and Jain, M.: Review of optically stimulated luminescence (OSL) instrumental developments for retrospective dosimetry, Radiat. Meas., 45, 253-257, 2010.

Boulton, G.S.: Processes of glacier erosion on different substrata, J. Glaciol., 23, 15-38, 1979.

520

Briner, J.P., and Swanson, T.W.: Using inherited cosmogenic [36]Cl to constrain glacial erosion rates of the Cordilleran ice sheet, Geology, 26, 3-6, 1998.

Brown, N.D., and Moon, S.: Revisiting erosion rate estimates from luminescence profiles in exposed bedrock

525 surfaces using stochastic erosion simulations, Earth Planet. Sc. Lett., 528, 115842, 2019.

Christl, M., Vockenhuber, C., Kubik, P.W., Wacker, L., Lachner, J., Alfimov, V., and Synal, H.A.: The ETH Zurich AMS facilities: performance parameters and reference materials, Nucl. Instrum. Meth. B, 294, 29-38, 2013.

530   Claude, A., Ivy-Ochs, S., Kober, F., Antognini, M., Salcher, B., and Kubik, P.W.: The Chironico landslide
        (Valle Leventina, southern Swiss Alps): age and evolution, Swiss J. Geosci., 107, 273-291, 2014.

        Cogez, A., Meynadier, L., Allègre, C., Limmois, D., Herman, F., and Gaillardet, J.: Constraints on the role of
        tectonic and climate on erosion revealed by two time series analysis of marine cores around New Zealand, Earth
535   Planet. Sc. Lett., 410, 174-185, 2015.

        Cook, S.J., Swift, D.A., Kirkbride, M.P., Knight, P.G., and Waller, R.I.: The empirical basis for modelling
        glacial erosion rates, Nat. Commun., 11, 759, 2020.

540   Cowton, T., Nienow, P., Batholomew, I., Sole, A., and Mair, D.: Rapid erosion beneath the Greenland ice sheet,
        Geology, 40, 343-346, 2012.

        Dahl, R.: Post-glacial micro-weathering of bedrock surfaces in the Narvik district of Norway, Geogr. Ann. A.,
        49, 155-166, 1967.
545
        Delmas, M., Calvet, M., and Gunnell, Y.: Variability of Quaternary glacial erosion rates- A global perspective
        with special reference to the Eastern Pyrenees, Quaternary Sci. Rev., 28(5-6), 484-498, 2009.

        Dornbusch, U., Moses, C., Robinson, D.A., and Williams, R.: Soft copy photogrammetry to measure shore
550   platform erosion on decadal time scales, J. Coast. Conserv., 11, 193-200, 2008.

        Dunai, T.J.: Cosmogenic Nuclides: Principles, Concepts and Applications in the Earth Surface Sciences,
        Cambridge University Press, Cambridge, 2010.

555   Durcan, J.A., King, G.E., and Duller, G.A.T.: DRAC: Dose Rate and Age Calculator for trapped charge dating,
        Quat. Geochronol., 28, 54-61, 2015.

        Elkadi, J., King, G.E., Lehmann, B., and Herman, F.: Reducing variability in OSL rock surface dating profiles,
        Quat. Geochronol., 64, 101169, 2021.
560
        Embleton, C., and King, C.A.M.: Glacial and Periglacial Geomorphology, Edward Arnold: London, 1975.

        Fabel, D., Harbor, J., Dahms, D., James, A., Elmore, D., Horn, L., Daley, K., and Steele, C.: Spatial patterns of
        glacial erosion at a valley scale derived from terrestrial cosmogenic [10]Be and [26]Al concentrations in rock, Ann.
565   Assoc. Am. Geogr., 94, 241-255, 2004.

Freiesleben, T., Sohbati, R., Murray, A.S., Jain, M., al Khasawneh, S., Hvidt, S., and Jakobsen, B.:
Mathematical model quantifies multiple daylight exposure and burial events for rock surfaces using
570   luminescence dating, Radiat. Meas., 81, 16–22, 2015.

Gliganic, L.A., Meyer, M.C., Sohbati, R., Jain, M., and Barrett, S.: OSL surface exposure dating of a lithic
quarry in Tibet: laboratory validation and application, Quat. Geochronol., 49, 199–204, 2019.

575   GLIMS Consortium: GLIMS Glacier Database, Version 1. [Analysis_IDs 85831--86727, Paul, Frank
(submitter); Paul, Frank (analyst(s))]. Boulder, Colorado, USA. NASA National Snow and Ice. Data Center
Distributed Active Archive Center, 2005.

GLIMS Consortium: GLIMS Glacier Database, Version 1. [Analysis_IDs 165649--167068, Fischer, Mauro
580   (submitter); Fischer, Mauro (analyst(s))]. Boulder, Colorado, USA. NASA National Snow and Ice. Data Center
Distributed Active Archive Center, 2005.

GLIMS Consortium: GLIMS Glacier Database, Version 1. [Analysis_IDs 328449--335984, Paul, Frank
(submitter); Paul, Frank (analyst(s))]. Boulder, Colorado, USA. NASA National Snow and Ice. Data Center
585   Distributed Active Archive Center, 2005.

GLIMS Consortium: GLIMS Glacier Database, Version 1. [Analysis_IDs 336896--338862, Paul, Frank
(submitter); Maisch, Max (analyst(s))]. Boulder, Colorado, USA. NASA National Snow and Ice. Data Center
Distributed Active Archive Center, 2005.
590

GLIMS Consortium: GLIMS Glacier Database, Version 1. [Analysis_IDs 338863--340868, Fischer, Mauro
(submitter); Fischer, Mauro (analyst(s))]. Boulder, Colorado, USA. NASA National Snow and Ice. Data Center
Distributed Active Archive Center, 2005.

595   GLIMS Consortium: GLIMS Glacier Database, Version 1. [Analysis_IDs 341659--343718, Maisch, Max
(submitter); Benz, Christof; Wipf, Andreas (analyst(s))]. Boulder, Colorado, USA. NASA National Snow and
Ice. Data Center Distributed Active Archive Center, 2005.

Goehring, B.M., Schaefer, J.M., Schluechter, C., Lifton, N.A., Finkel, R.C., Timothy Jull, A.J., Akçar, N., and
600   Alley, R.B.: The Rhone Glacier was smaller than today for most of the Holocene, Geology, 39 (7), 679-692,
2011.

Gosse, J.C., and Phillips, F.M.: Terrestrial in situ cosmogenic nuclides: theory and application, Quaternary Sci.
Rev., 20, 1475-1560, 2001.
605

Guillon, H., Mugnier, J.-L., Buoncristiani, J.-F., Carcaillet, J., Godon, C., Prud'homme, C., van der Beek, P.,
and Vassallo, R.: Improved discrimination of subglacial and periglacial erosion using ^{10}Be concentration

measurements in subglacial and supraglacial sediment load of the Bossons glacier (Mont Blanc massif, France),
Earth Surf. Process. Landf., 40(9), 2015.

610

Habermann, J., Schilles, T., Kalchgruber, R., and Wagner, G.A.: Steps towards surface dating using
luminescence, Radiat. Meas., 32, 847–851, 2000.

Hallet, B., Hunter, L., and Bogen, J.: Rates of erosion and sediment evacuation by glaciers: A review of field
615   data and their implications, Glob. Planet. Change, 12, 213-235, 1996.

Harbor, J.M.: Numerical modeling of the development of U-shaped valleys by glacial erosion, Geol. Soc. Am.
Bull., 104, 1364-1375, 1992.

620   Heimsath, A.M. and McGlynn, R.: Quantifying periglacial erosion in the Nepal high Himalaya,
Geomorphology, 97, 5-23, 2007.

Herman, F., Seward, D., Valla, P.G., Carter, A., Kohn, B., Willet, S.D., and Ehlers, T.A.: Worldwide
acceleration of mountain erosion under a cooling climate, Nature, 504, 423-426, 2013.

625

Herman, F., Beyssac, O., Brughelli, M., Lane, S.T., Leprince, S., Adatte, T., Lin, J.Y.Y., Avouac, J.-P., and
Cox, S.C.: Erosion by an Alpine glacier, Science, 350, 193-195, 2015.

Herman, F. and Champagnac, J.-D.: Plio-Pleistocene increase of erosion rates in mountain belts in response to
630   climate change, Terra Nova, 28, 2-10, 2016.

Herman, F., Braun, J., Deal, E., and Prasicek, G.: The response time of glacial erosion, J. Geophys. Res. Earth
Surf., 123, 801-817, 2018.

635   Herman, F. and King, G.E.: Luminescence Thermochronometry: Investigating the Link between Mountain
Erosion, Tectonics and Climate, Elements, 14, 33-38, 2018.

Herman, F., De Doncker, F., Delaney, I., Prasicek, G., and Koppes, M.: The impact of glaciers on mountain
erosion, Nat. Rev. Earth Environ., 2, 422-435, 2021.

640

Holzhauser, H.: Gletscherschwankungen innerhalb der letzten 3200 Jahre am Beispiel des grossen Aletsh- und
des Gorner- gletschers. Neue Ergebniss, Gletscher im ständigen Wandel, 101-123, 1995.

Holzhauser, H.: Zur Geschichte des Gornergletschers ein Puzzle aus historischen Dokumenten und fossilen
645   Hölzern aus dem Gletschervorfeld. Bern: Geographisches Institut der Universität Bern, 2010.

Hormes, A., Müller, B.U., and Schlüchter, C.: The Alps with little ice: evidence for eight Holocene phases of reduced glacier extent in the Swiss Alps, Holocene, 11, 255-265, 2001.

650 Humphrey, N.F. and Raymond, C.: Hydrology, erosion and sediment production in a surging glacier: Variegated Glacier, Alaska, 1982-1983, J. Glaciol., 40, 539-552, 1994.

Huntley, D.J., McMullan, W.G., Godfrey-Smith, D.I., and Thewalt, M.L.W.: Time-dependent recombination spectra arising from optical ejection of trapped charges in feldspars, J. Lumin., 44, 41–46, 1989.

655

Huntley, D.J.: An explanation of the power-law decay of luminescence, J. Phys. Condens. Matter, 18, 1359-1365, 2006.

Inkpen, R.J. and Jackson, J.: Contrasting weathering rates in coastal, urban and rural areas in southern Britain:
660 preliminary investigations using gravestones, Earth Surf. Process. Landf., 25, 229-238, 2000.

Inkpen, R.J., Collier, P., and Fontana, D.J.L.: Close-range photogrammetric analysis of rock surfaces, Zeitschrift für Geomorphologie, 120, 67-81, 2000.

665 Ivy-Ochs, S.: The Dating of Rock Surfaces Using in Situ Produced ^{10}Be, ^{26}Al and ^{36}Cl, with examples from Antarctica and the Swiss Alps (PhD Thesis), ETH, Zurich, 1996.

Ivy-Ochs, S., Kerschner, H., Maisch, M., Christl, M., Kubik, and P.W., Schlüchter, C.: Latest Pleistocene and Holocene glacier variations in the European Alps, Quaternary Sci. Rev., 28, 21-22, 2009.

670

Ivy-Ochs, S. and Briner, J.P.: Dating Disappearing Ice with Cosmogenic Nuclides, Elements, 10(5), 351-356, 2014.

Jenkins, G.T.H., Duller, G.A.T., Roberts, H.M., Chiverrell, and R.C., Glasser, N.F.: A new approach for
675 luminescence dating glaciofluvial deposits- high precision optical dating of cobbles, Quaternary Sci. Rev., 192, 263–273, 2018.

Kars, R.H., Wallinga, J., and Cohen, K.M.: A new approach towards anomalous fading correction for feldspar IRSL dating- tests on samples in field saturation, Radiat. Meas., 43(2-6), 786-790, 2008.

680

Kirkbride, M.P. and Bell, C.M.: Edge roundness of boulders of Torridonian Sandstone (northwest Scotland): Applications for relative dating and implications for warm and cold climate weathering rates, Boreas, 39, 187-198, 2010.

685 Kohl, C.P. and Nishiizumi, K.: Chemical isolation of quartz for measurement of in-situ produced cosmogenic nuclides, Geochim.Cosmochim. Ac., 56, 3583-3587, 1992.

Koppes, M. and Montgomery, D.: The relative efficacy of fluvial and glacial erosion over modern to orogenic timescales, Nat. Geosci., 2, 644-647, 2009.

690

Koppes, M., Hallet, B., Rignot, E., Mouginot, J., Smith Wellner, J., and Boldt, K.: Observed latitudinal variations in erosion as a function of glacier dynamics, Nature, 526, 100-103, 2015.

Kronig, O., Ivy-Ochs, S., Hajdas, I., Christl, M., Wirsig, C., and Schlüchter, C.: Holocene evolution of the Triftje- and the Oberseegletscher (Swiss Alps) constrained with [10]Be exposure and radiocarbon dating, Swiss J. Geosci., 111, 117-131, 2017.

695

Laj, C., Kissel, C., and Beer, J.: High resolution global Paleointensity Stack since 75 kyr (GLOPIS-75) calibrated to Absolute values, Timescales Paleomagnetic Field, Geoph. Monog. Series, 145, 255-265, 2004.

700

Lal. D.: Cosmic ray labelling of erosion surfaces: in situ nuclide production rates and erosion models, Earth and Planet. Sc. Lett., 104, 424-439, 1991.

Lapp, T., Kook, M.H., Murray, A.S., Thomsen, K.J., Buylaert, J.-P., and Jain, M.: A new luminescence detection and stimulation head for the Risø TL/OSL reader, Radiat. Meas., 81, 178-184, 2015.

705

Laskaris, N. and Liritzis, I.: A new mathematical approximation of sunlight attenuation in rocks for surface luminescence dating, J. Lumin., 131, 1874–1884, 2011.

Lehmann, B., Valla, P.G., King, G.E., and Herman, F.: Investigation of OSL surface exposure dating to reconstruct post-LIA glacier fluctuations in the French Alps (Mer de Glace, Mont Blanc massif), Quat. Geochronol., 44, 64–74, 2018.

710

Lehmann, B., Herman, F., Valla, P.G., King, G.E., and Biswas, R.H.: Evaluating post-glacial bedrock erosion and surface exposure duration by coupling in-situ OSL and [10]Be dating, Earth Surf. Dyn., 7, 633-662, 2019.

715

Lehmann, B., Herman, F., Valla, P.G., King, G.E., Biswas, R.H., Ivy-Ochs, S., Steinemann, O., and Christl, M.: Postglacial erosion of bedrock surfaces and deglaciation timing: new insights from the Mont Blanc massif (Western Alps), Geology, 48 (2), 139–144, 2020.

720

Leith, K., Moore, J.R., Amann, F., and Loew, S.: Sub-glacial extensional fracture development and implications for Alpine valley evolution, J. Geophys. Res. Earth Surf., 119, 62-81, 2014.

Lifton, N.A., Sato, T., and Dunai, T.J.: Scaling in situ cosmogenic nuclide production rates using analytical approximations to atmospheric cosmic-ray fluxes, Earth Planet. Sc. Lett., 386, 149-160, 2014.

725

Liu, J., Cui, F., Murray, A.S., Sohbati, R., Jain, M., Gao, H., Li, W., Li, C., Li, P., Zhou, T., and Chen, J.: Resetting of the luminescence signal in modern riverbed cobbles along the course of the Shiyang River, China, Quat. Geochronol., 49, 184–190, 2019.

730

Lupker, M., France-Lanord, C., Galy, V., Lavé, J., and Kudrass, H.: Increasing chemical weathering in the Himalayan system since the Last Glacial Maximum, Earth Planet. Sc. Lett., 365, 243-252, 2013.

Martin, L.C.P., Blard, P.-H., Balco, G., Lave, J., Delunel, R., Lifton, N., and Laurent, V.: The CRep program
735   and the ICE-D production rate calibration database: A fully parameterizable and updated online tool to compute cosmic ray exposure ages, Quat. Geochronol., 38, 25-49, 2017.

Meyer, M.C., Gliganic, L.A., Jain, M., Sohbati, R., and Schmidmair, D.: Lithological controls on light penetration into rock surfaces- implications for OSL and IRSL surface exposure dating, Radiat. Meas., 120,
740   298-304, 2018.

Molnar, P.: Late Cenozoic increase in accumulation rates of terrestrial sediment: How Might Climate Change Have Affected Erosion Rates?, Annu. Rev. Earth Planet. Sci., 32, 67-89, 2004.

745   Montgomery, D.R.: Valley formation by fluvial and glacial erosion, Geology, 30, 1047-1050, 2002.

Moses, C., Robinson, D., and Barlow, J.: Methods for measuring rock surface weathering and erosion: a critical review, Earth Sci. Rev., 135, 141-161, 2014.

750   Nicholson, D.T.: Rock control on microweathering of bedrock surfaces in a periglacial environment, Geomorphology, 101, 655-665, 2008.

Nishiizumi, K., Lal, D., Klein, J., Middleton, R., and Arnold, J.: Production of [10]Be and [26]Al by cosmic rays in terrestrial quartz in-situ and implications for erosion rates, Nature, 319, 134-136, 1986.

755

Nishiizumi, K., Imamura, M., Caffee, M. W., Southon, J.R., Finkel, R.C., and McAninch, J.: Absolute calibration of [10]Be AMS standards, Nucl. Instrum. Meth. B, 258, 403-413, 2007.

O'Farrell, C.R., Heimsath, A.M., Lawson, D.E., Jorgensen, L.M., Evenson, E.B., Larson, G., and Denner, J.:
760   Quantifying periglacial erosion: insights on a glacial sediment budget, Matanuska Glacier, Alaska, Earth Surf. Process. Landf., 34(15), 2008-2022, 2009.

Oerlemans, J. and Grisogono, B.: Glacier winds and parametrisation of the related surface heat fluxes, Tellus A: Dyn. Meteorol. Oceanogr., 54, 440-452, 2002.

765

Ou, X.J., Roberts, H.M., Duller, G.A.T., Gunn, M.D., and Perkins, W.T.: Attenuation of light in different rock types and implications for rock surface luminescence dating, Radiat. Meas., 120, 305-311, 2018.

Pavon-Carrasco, F. J., Osete, M. L., Torta, J. M., and De Santis, A.: A geomagnetic field model for the

770   Holocene based on archaeomagnetic and lava flow data, Earth Planet. Sc. Lett., 388, 98-109, 2014.

Polikreti, K., Michael, C., and Maniatis, Y.: Authenticating marble sculptures with thermoluminescence, Ancient TL, 20, 11–18, 2002.

775   Polikreti, K., Michael, C.T., and Maniatis, Y.: Thermoluminescence characteristics of marble and dating of freshly excavated marble objects, Radiat. Meas., 37, 87–94, 2003.

Portenga, E.W. and Bierman, P.R.: Understanding the Earth's eroding surface with [10]Be, GSA Today, 21(8), 4-10, 2011.

780

Protin, M., Schimmelpfennig, I, Mugnier, J.-L., Ravanel, L., Le Roy, M., Deline, P., Favier, V., and Buoncristiani, J.-F.: Climatic reconstructions for the Younger Dryas/Early Holocene transition and the Litte Ice Age based on paleo-extents of Argentière glacier (French Alps), Quaternary Sci. Rev., 221, 105863, 2019.

785   Raup, B.H., Racoviteanu, A., Khalsa, S.J.S., Helm, C., Armstrong, R., Arnaud, Y.: The GLIMS Geospatial Glacier Database: a new tool for studying glacier change, Global Planet. Change, 56, 101-110, 2007.

Reiners, P.W. and Brandon, M.T.: Using Thermochronology to Understand Orogenic Erosion, Annu. Rev. Earth Planet. Sci., 34, 419–466, 2006.

790

Riihimaki, C.A., MacGregor, K.R., Anderson, R.S., Anderson, S.P., and Loso, M.G.: Sediment evacuation and glacial erosion rates at a small alpine glacier, J. Geophys. Res. Earth Surf., 110, F03003, 2005.

Ruszkiczay-Rüdiger, Z., Kern, Z., Urdea, P., Madarász, B., Braucher, R., ASTER Team.: Limited glacial

795   erosion during the last glaciation in mid-latitude cirques (Retezat Mts, Southern Carpathians, Romania), Geomorphology, 384, 107719, 2021.

Schimmelpfennig, I., Schaefer, J.M., Akcar, N., Koffman, T., Ivy-Ochs, S., Schwartz, R., Finkel, R.C., Zimmerman, S., and Schlüchter, C.: A chronology of Holocene and Little Ice Age glacier culminations of the

800   Steingletscher, Central Alps, Switzerland based on high-sensitivity beryllium-10 moraine dating, Earth Planet. Sc. Lett., 393, 220-230, 2014.

Small, E.E., Anderson, R.S., Repka, J.L., and Finkel, R.: Erosion rates of alpine bedrock summit surfaces deduced from in situ [10]Be and [26]Al, Earth Planet. Sc. Lett., 150, 413-425, 1997.

805

Sohbati, R., Murray, A.S., Jain, M., Buylaert, J.-P., and Thomsen, K.: Investigating the resetting of OSL signals in rock surfaces, Geochronometria, 38(3), 249–258, 2011.

Sohbati, R., Murray, A.S., Chapot, M.S., Jain, M., Pederson, J.: Optically stimulated luminescence (OSL) as a
810   chronometer for surface exposure dating, J. Geophys. Res. Solid Earth, 117, B09202, 2012.

Sohbati, R., Murray, A.S., Jain, M., and Avner, U.: Age of a prehistoric "Rodedian" cult site constrained by sediment and rock surface dating techniques, Quat. Geochronol., 30, 90–99, 2015.

815   Sohbati, R., Liu, J., Jain, M., Murray, A., Egholm, D., Paris, R., and Guralnik, B.: Centennial- to millennial-scale hard rock erosion rates deduced from luminescence-depth profiles, Earth Planet. Sc. Lett., 493, 218-230, 2018.

Solomina, O.N., Bradley, R.S., Hodgson, D.A., Ivy-Ochs, S., Jomelli, V., Mackintosh, A.N., Nesje, A., Owen,
820   L.A., Wanner, H., Wiles, G.C., and Young, N.E.: Holocene glacier fluctuations, Quaternary Sci. Rev., 111, 9-34, 2015.

Steinemann, O., Ivy-Ochs, S., Hippe, K., Christl, M., Haghipour, N., and Synal, H.-A.: Glacial erosion by the Trift glacier (Switzerland): Deciphering the development of riegels, rock basins and gorges, Geomorphology,
825   375, 107533, 2021.

Stroeven, A.P., Harbor, J., Fabel, D., Kleman, J., Hättestrand, C., Elmore, D., Fink, D., and Fredin, O.: Slow, patchy landscape evolution in northern Sweden despite repeated ice-sheet glaciation, Geol. Soc. Am. Spec. Pap., 398, 387, 2006.
830
Turowski, J.M. and Cook, K.L.: Field techniques for measuring bedrock erosion and denudation. Earth Surf. Proc. Land., 42, 109-127, 2017.

Uppala, S. M., Kallberg, P. W., Simmons, A. J., Andrae, U., Bechtold, V. D. C., Fiorino, M., Gibson, J. K.,
835   Haseler, J., Hernandez, A., Kelly, G. A., Li, X., Onogi, K., Saarinen, S., Sokka, N., Allan, R. P., Andersson, E., Arpe, K., Balmaseda, M. A., Beljaars, A. C. M., Van De Berg, L., Bidlot, J., Bormann, N., Caires, S., Chevallier, F., Dethof, A., Dragosavac, M., Fisher, M., Fuentes, M., Hagemann, S., Holm, E., Hoskins, B.J., Isaksen, L., Janssen, P. A. E. M., Jenne, R., Mcnally, A. P., Mahfouf, J.-F., Morcrette, J.-J., Rayner, N. A., Saunders, R. W., Simon, P., Sterl, A., Trenberth, K. E., Untch, A., Vasiljevic, D., Viterbo, P., and Woollen, J.:
840   The ERA-40 re-analysis, Q. J. Royal Meteor Soc., 131, 2961-3012, 2005.

Vafiadou, A., Murray, A., and Liritzis, I. : Optically stimulated luminescence (OSL) dating investigations of rock and underlying soil from three case studies, J. Archaeol. Sci., 34, 1659-1669, 2007.

845   Willenbring, J.K. and von Blanckenburg, F.: Long-term stability of global erosion rates and weathering during late-Cenozoic cooling. Nature, 465, 211-214, 2010.

Willenbring, J.K. and Jerolmack, D.J.: The null hypothesis: Globally steady rates of erosion, weathering fluxes and shelf sediment accumulation during Late Cenozoic mountain uplift and glaciation, Terra Nova, 28, 11-18, 850   2016.

Wirsig, C., Zasadni, J., Christl, M., Akçar, N., and Ivy-Ochs, S.: Dating the onset of LGM ice surface lowering in the High Alps, Quaternary Sci. Rev., 143, 37-50, 2016a.

855   Wirsig, C.: Constraining the timing of deglaciation of the High Alps and rates of subglacial erosion with cosmogenic nuclides (PhD dissertation No. 22978), ETH, Zurich, 2016b.

Wirsig, C., Ivy-Ochs, S., Reitner, J.M., Christl, M., Vockenhuber, C., Bichler, M., and Reindl, M.: Subglacial abrasion rates at Goldbergkees, Hohe Tauern, Austria, determined from cosmogenic [10]Be and [36]Cl 860   concentrations, Earth Surf. Proc. Land., 42(7), 1119-1131, 2017.

Young, N.E., Briner, J.P., Maurer, J., and Schaefer, J.M.: [10]Be measurements in bedrock constrain erosion beneath the Greenland Ice Sheet margin, Geophys. Res. Lett., 43, 11708-11719, 2016.

865   Zhang, P., Molnar, P. and Downs, W.R.: Increased sedimentation rates and grain sizes 2-4 Myr ago due to the influence of climate change on erosion rates, Nature, 410, 891–897, 2001.